Biophysical Journal
Biophysical Letter

Biophysical Society

On the Mechanism of Bilayer Separation by Extrusion, or Why Your LUVs Are Not Really Unilamellar

Haden L. Scott,[1,2] Allison Skinkle,[3,4] Elizabeth G. Kelley,[5] M. Neal Waxham,[6] Ilya Levental,[4,*] and Frederick A. Heberle[1,4,*]

[1]Center for Environmental Biotechnology, University of Tennessee, Knoxville, Tennessee; [2]Shull Wollan Center, Oak Ridge National Laboratory, Oak Ridge, Tennessee; [3]Department of Biosciences, Rice University, Houston, Texas; [4]Department of Integrative Biology and Pharmacology, University of Texas Health Science Center, Houston, Texas; [5]NIST Center for Neutron Research, National Institute of Standards and Technology, Gaithersburg, Maryland; and [6]Department of Neurobiology and Anatomy, University of Texas Health Science Center, Houston, Texas

ABSTRACT Extrusion through porous filters is a widely used method for preparing biomimetic model membranes. Of primary importance in this approach is the efficient production of single bilayer (unilamellar) vesicles that eliminate the influence of interlamellar interactions and strictly define the bilayer surface area available to external reagents such as proteins. Submicroscopic vesicles produced using extrusion are widely assumed to be unilamellar, and large deviations from this assumption would impact interpretations from many model membrane experiments. Using three probe-free methods—small angle X-ray and neutron scattering and cryogenic electron microscopy—we report unambiguous evidence of extensive multilamellarity in extruded vesicles composed of neutral phosphatidylcholine lipids, including for the common case of neutral lipids dispersed in physiological buffer and extruded through 100-nm diameter pores. In such preparations, only ~35% of lipids are externally accessible and this fraction is highly dependent on preparation conditions. Charged lipids promote unilamellarity as does decreasing solvent ionic strength, indicating the importance of electrostatic interactions in determining the lamellarity of extruded vesicles. Smaller extrusion pore sizes also robustly increase the fraction of unilamellar vesicles, suggesting a role for membrane bending. Taken together, these observations suggest a mechanistic model for extrusion, wherein the formation of unilamellar vesicles involves competition between bilayer bending and adhesion energies. The findings presented here have wide-ranging implications for the design and interpretation of model membrane studies, especially ensemble-averaged observations relying on the assumption of unilamellarity.

SIGNIFICANCE Extruded vesicles are a ubiquitous tool in membrane research. It is widely presumed that extrusion produces unilamellar (i.e., single bilayer) vesicles, an assumption that is often crucial for data analysis and interpretation. Using X-ray and neutron scattering and cryogenic electron microscopy, we show that a substantial amount of lipid remains inaccessible after extrusion because of an abundance of multilamellar vesicles (MLVs). Although this is a general phenomenon for neutral lipids, MLV contamination can be reduced by several complementary approaches, such as including charged lipids in the mixture, reducing the ionic strength of the aqueous medium, and reducing the extrusion pore size. These observations together suggest a mechanism by which extrusion strips MLVs of their layers.

Biomimetic model membranes enable carefully controlled, systematic experiments that can inform on complex functionality in living membranes. Many insights into biological membrane structure (1,2), shape transformations (3), dynamics (4), and phase behavior (5–7) derive from studies of chemically defined synthetic bilayers. These systems have also contributed greatly to our understanding of the interactions between proteins and biomembranes (8).

Although synthetic membranes can be produced in a variety of sizes and geometries, perhaps the most widely used experimental system consists of extruded vesicles with diameters on the order of 100 nm. These vesicles are smaller than the resolution limit of light microscopy, but their size distributions can be measured with dynamic light scattering (DLS). Because of their uniform size and physical

Submitted June 12, 2019, and accepted for publication September 10, 2019.

*Correspondence: ilya.levental@uth.tmc.edu or fheberle@utk.edu

Frederick A. Heberle's present address is Department of Chemistry, University of Tennessee, Knoxville, Tennessee.

Editor: Joseph Zasadzinski.

https://doi.org/10.1016/j.bpj.2019.09.006

properties, extruded vesicles are readily amenable to ensemble-averaged spectroscopic and scattering techniques as well as a vast array of biochemical assays. For many experiments, a convenient assumption is that half of the total lipid is exposed to the external solvent, where it can interact with reagents in the extravesicular space. Unfortunately, few techniques are directly sensitive to the presence of inaccessible lipid layers in vesicle samples. Instead, uniformity in vesicle size distributions is often taken as evidence of successful extrusion and, consequently, of a sufficiently unilamellar sample; indeed, such preparations are typically referred to as large unilamellar vesicles. In this letter, we show that the assumption of unilamellarity is incorrect for many commonly used vesicle formulations.

Fig. 1 *A* shows small angle X-ray scattering (SAXS) intensity versus momentum transfer q for 1-palmitoyl-2-oleoyl-sn-glycero-3-phosphocholine (POPC) dispersions in phosphate-buffered saline (PBS) buffer at 25°C (all membranes in this study are measured in the fluid lamellar phase). Without extrusion, a characteristic set of broad, equally spaced peaks (in this case, at $q = 0.10$, 0.20, and 0.30 $Å^{-1}$) emerges from lobes of diffuse scattering. These peaks are the first three orders of Bragg reflections from a repeating structure in the sample with a spacing of $d = 2\pi/q_1 = 62.6$ Å. Given the well-known tendency of lipid films to swell into multilamellar vesicles (MLVs) consisting of multiple concentric bilayers separated by water, the observation of Bragg peaks corresponding to the lamellar repeat distance (i.e., one bilayer plus an interstitial water layer) is expected. The surprising result is that standard extrusion protocols believed to produce 100-nm unilamellar vesicles do not eliminate these reflections (Fig. 1 *A*). Though the peaks in the extruded vesicle sample are broader and less intense, their prominence indicates that substantial multilamellar structures remain even after extrusion.

We confirmed the presence of MLVs in both nonextruded (Fig. 1 *B*) and extruded (Fig. 1 *C*) samples by direct, real-space cryogenic electron microscopy (cryoEM) imaging. MLVs and unilamellar vesicles in the extruded sample are comparable in size (Fig. 1 *C*), suggesting that all vesicles passed through the extrusion pores (as opposed to leaking through the filter edges) and emphasizing that a uniform size distribution in DLS measurements does not imply the absence of MLVs in extruded samples. Indeed, we find that the extent of lamellarity (determined from SAXS data as described below) is only weakly correlated with average vesicle size and is not correlated with the size polydispersity, both determined from DLS (Fig. S1; Table S2).

The combination of Bragg peaks in scattering data and direct observation in cryoEM images provides unambiguous proof of multilamellar structures in extruded vesicle preparations, an outcome that is usually undesirable and often overlooked. To quantify the extent of multilamellarity, scattering data were fit to a model combining a single lipid bilayer form factor and a multilamellar structure factor parameterized with a modified exponential distribution for the number of lamellae (see Supporting Materials and Methods, Section S1 for details of the model and fit procedure). The solid lines in Fig. 1 *A* demonstrate that the model successfully captures both the diffuse lobes of scattering originating from the bilayer structure as well as the broad

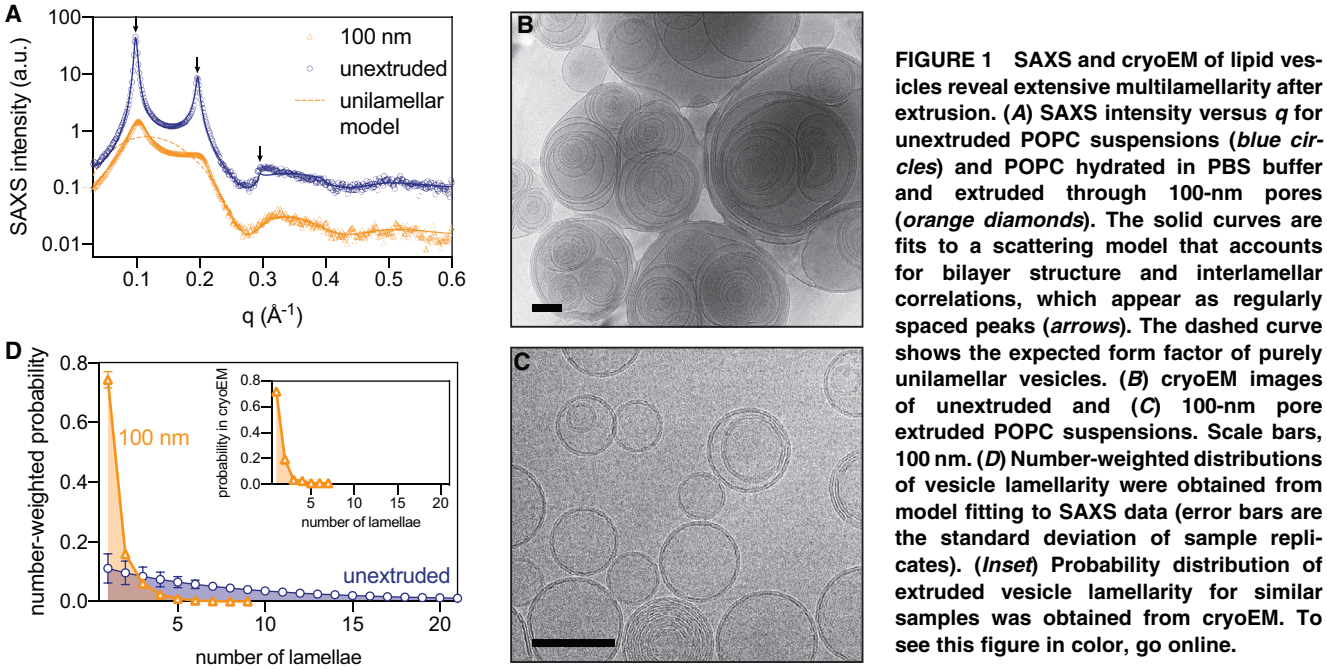

FIGURE 1 SAXS and cryoEM of lipid vesicles reveal extensive multilamellarity after extrusion. (*A*) SAXS intensity versus *q* for unextruded POPC suspensions (*blue circles*) and POPC hydrated in PBS buffer and extruded through 100-nm pores (*orange diamonds*). The solid curves are fits to a scattering model that accounts for bilayer structure and interlamellar correlations, which appear as regularly spaced peaks (*arrows*). The dashed curve shows the expected form factor of purely unilamellar vesicles. (*B*) cryoEM images of unextruded and (*C*) 100-nm pore extruded POPC suspensions. Scale bars, 100 nm. (*D*) Number-weighted distributions of vesicle lamellarity were obtained from model fitting to SAXS data (error bars are the standard deviation of sample replicates). (*Inset*) Probability distribution of extruded vesicle lamellarity for similar samples was obtained from cryoEM. To see this figure in color, go online.

reflections generated by the lattice of stacked lamellae. The dashed line shows the expected scattering from purely unilamellar vesicles. Fig. 1 *D* compares distributions of the number of lamellae obtained from SAXS analysis to those obtained by counting ~100 vesicles in cryoEM images, revealing excellent agreement between these approaches. As expected, unextruded vesicles showed a wide distribution that narrows and shifts toward fewer lamellae upon extrusion; however, only half of the lipid mass in the extruded sample (53 ± 4%) is in unilamellar structures, as determined from four replicate samples of POPC in PBS buffer (Table S2).

Lamellar distributions enable a straightforward estimate of the fraction of externally accessible lipid f_{acc} (see Supporting Materials and Methods, Section S1 for details). This parameter is crucial for many experiments as it reports directly on the fraction of total lipid accessible to externally added reagents, such as proteins, quenchers, or small molecules. A perfectly unilamellar vesicle sample would have approximately half of its total lipid exposed on the vesicle surface ($f_{acc} \approx 0.5$). Fig. 2 shows that common preparations (e.g., 100 nm vesicles of phosphocholine (PC) lipid hydrated in physiological buffer) yield $f_{acc} = 0.35$, ~30% lower than expected for a unilamellar sample. Put another way, approximately one-third of the lipids expected to be accessible to external reagents are instead entrained in vesicle lumens.

We observed qualitative agreement between f_{acc} calculated from SAXS and cryoEM images (stars in Fig. 2). Images also revealed unexpected complexity, including bilamellar structures consisting of larger vesicles enveloping smaller "nested" vesicles (Fig. 2 *B*, arrowhead), which comprised ~20% of 100 nm POPC vesicles (Fig. 2 *C*). Scattering analyses likely do not fully capture the abundance of these structures, which manifest in $I(q)$ as a gentle oscillation in the low-q regime in which the intensity is also influenced by vesicle concentration and size distribution, making it difficult to unambiguously assign scattering features. These nested structures likely explain why f_{acc} reported by cryoEM was systematically lower than estimates from SAXS (Fig. 2 *A*).

It has previously been reported that a small amount of charged lipid can reduce or eliminate Bragg reflections in scattering data (9,10). Hypothesizing that interlamellar repulsion would promote unilamellarity, we investigated the influence of charged lipids and buffer ionic strength on f_{acc}. Inclusion of negatively charged 1-palmitoyl-2-oleoyl-sn-glycero-3-phosphorylglycerol (POPG) in POPC bilayers at concentrations up to 10 mol% decreased multilamellarity and increased lipid exposure, as evidenced by both SAXS and cryoEM (Figs. 2, *A* and *C* and S2; Table S2), with a similar effect observed in small angle neutron scattering (SANS) data from 1,2-dimyristoyl-sn-glycero-3-phosphocholine (DMPC)/1,2-dimyristoyl-sn-glycero-3-phosphorylglycerol bilayers (Fig. S3 *B*; Table S3). Greater unilamellarity (i.e., higher f_{acc}) was also achieved without changing membrane lipid composition but instead by reducing solvent ionic strength, as shown in Fig. 2 for POPC hydrated with water. The absence of screening counterions greatly increased f_{acc} even in vesicles composed of zwitterionic lipids with no net charge, and further inclusion of as little as 2 mol% POPG or 1-palmitoyl-2-oleoyl-sn-glycero-3-phospho-L-serine resulted in essentially purely unilamellar vesicles. In good agreement with SAXS, 93% of the POPG-containing vesicles extruded in water were unilamellar in cryoEM images (Fig. 2 *C*). Importantly, neither adding charged lipid at <10 mol% nor changing buffer composition caused significant changes to the area per lipid (Table S2), suggesting that overall bilayer structure was unaffected. Thus, although near-complete unilamellarity with minimal bilayer perturbation can be achieved in samples containing charged lipid and hydrated in pure

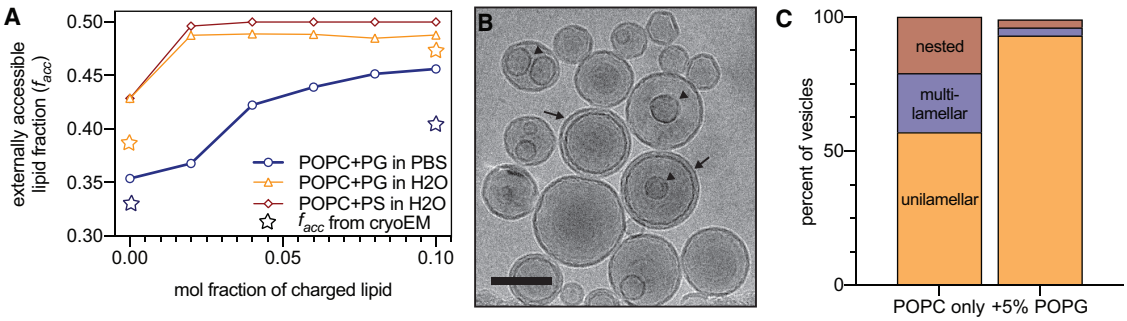

FIGURE 2 Unilamellarity increases with charged lipids and/or decreasing solvent ionic strength. (*A*) The fraction of externally accessible lipid f_{acc} (related to extent of unilamellarity) increases with an increasing abundance of charged lipid dopant (POPG or 1-palmitoyl-2-oleoyl-sn-glycero-3-phospho-L-serine (POPS)) in POPC bilayers extruded through 100-nm pores. Samples hydrated in PBS (*blue circles*) show a lower f_{acc} at all concentrations of charged lipid compared to hydration in pure water. Blue and orange stars represent f_{acc} calculated from cryoEM images of POPC in PBS and POPC plus PG in H_2O, respectively. (*B*) Shown is a typical cryoEM image of POPC vesicles extruded (100 nm) in water. Scale bars, 100 nm. Arrows highlight multilamellar structures, whereas arrowheads highlight nested vesicles. (*C*) Distribution of structures in 100 nm vesicles extruded in water were obtained from cryoEM. To see this figure in color, go online.

water, the absence of either factor yields a substantial amount of inaccessible lipid even after extrusion through 100-nm pores. Together, the effects of charged lipid and ionic strength point to a role for electrostatic repulsion in the production of unilamellar vesicles by extrusion.

We next investigated approaches to increase unilamellarity without altering the chemical composition of the bilayer or its aqueous solvent. Fig. 3 shows the influence of extrusion pore size for POPC bilayers with or without 5 mol% POPG (see also Fig. S4; Table S2). In both cases, decreasing the pore size increased the fraction of externally accessible lipid, with similar effects observed by SANS for 1,2-dilauroyl-sn-glycero-3-phosphocholine and DMPC (Figs. S3 *A* and S5; Table S3). The largest extrusion pore sizes (400 nm) produced vesicles that were difficult to categorize by cryoEM, containing complex multilamellar and nested structures (Fig. 3 *B*, left). In contrast, the smallest pore filters (30 or 50 nm) or sonication produced essentially unilamellar vesicles even in the absence of charged lipids, as evidenced by cryoEM (Fig. 3 *B*), SAXS (Fig. 3 *A*; Table S2), and SANS (Table S3). Taken together, these observations suggest an interplay between interlamellar repulsion and membrane curvature as key determinants of the efficiency of unilamellar extrusion.

Finally, we explored the influence of lipid chain structure on lamellarity. For eight different phosphatidylcholines, including saturated, unsaturated, and mixed chain species, f_{acc} ranged from 0.39 to 0.46 after extrusion through 100-nm pores (Fig. S6 *B*; Table S2). Surprisingly, egg sphingomyelin, also a neutral lipid, was significantly more unilamellar than any of the PC lipids (f_{acc} = 0.49). To explore the possible mechanisms underlying these results, we evaluated correlations between f_{acc} and membrane physical properties, including total number of carbons in the lipid chains, total number of double bonds in the chains, area per lipid, hydrocarbon thickness, melting temperature, and bending rigidity (Fig. S7; Table S5). The strongest correlation was with the bending energy: f_{acc} exhibits an approximately linear dependence on the bending modulus k_c determined from molecular simulations (11).

Taken together, the above results suggest a mechanism in which the lamellarity of an extruded sample is influenced by a competition between bilayer bending and adhesion energies. During extrusion, stacked bilayers must collectively bend to enter the cylindrical extrusion pore. Assuming mechanically uncoupled bilayers, the energy required to bend a multilamellar stack scales with both the number of bilayers and the membrane's bending rigidity and is inversely related to the radius of curvature. Rather than bending, one or more of the bilayers can instead separate from the stack and enter the pore with a smaller bending penalty, a process that is opposed by the interbilayer adhesion energy. Any factor that increases the cost of bending—for example, a larger intrinsic bending stiffness or a smaller pore radius—also increases the likelihood of lamellar separation. Similarly, any factor that lowers the bilayer adhesion energy, such as increasing interlamellar repulsion with charged lipids (12), also favors separation of layers and should therefore increase the fraction of unilamellar vesicles after extrusion. It is likely that the bending energy also contributes to an increased probability of unilamellar vesicles upon hydration (i.e., before extrusion), as recently proposed (13). Indeed, we found that the lipid with the largest bending modulus (egg sphingomyelin) had the greatest fraction of unilamellar vesicles both before and after extrusion (Table S2). However, sphingomyelin appears to be an outlier in this regard; for the PC lipids we examined, there was no correlation between f_{acc} before and after extrusion (Fig. S6; Table S2), suggesting that their final lamellar distribution depends predominantly on events occurring during extrusion.

The predictive power of the proposed mechanism relies on the ability to independently control interlamellar forces and bending rigidity, a requirement that is likely not strictly met in any real experiment. In some cases, the different influences reinforce each other; for example, it is well established that adding a charged lipid to neutral bilayers increases lamellar separation, which in turn reduces bilayer adhesion (14), and there is evidence that a charged lipid can also increase membrane bending rigidity

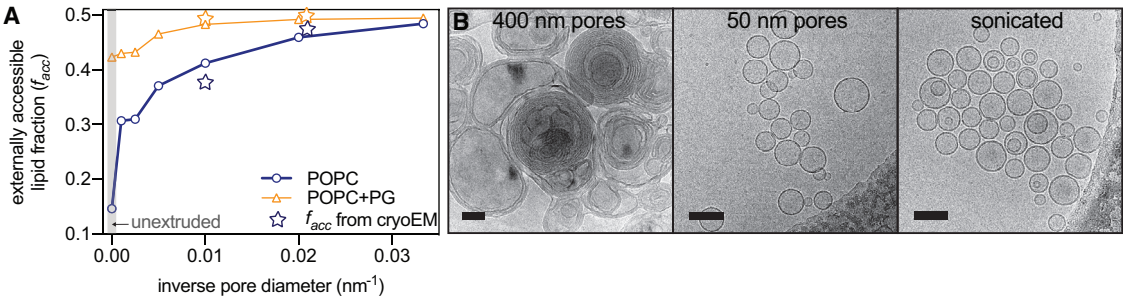

FIGURE 3 Unilamellarity increases with decreasing extrusion pore size. (A) The fraction of externally accessible lipid increases with decreasing extrusion pore size for POPC vesicles without (*blue circles*) or with (*orange triangles*) 5 mol% POPG. Stars represent f_{acc} calculated from cryoEM images. (*B*) Shown are typical cryoEM images of POPC vesicles extruded in water through 400- and 50-nm pore filters as well as after sonication. Scale bar, 100 nm. To see this figure in color, go online.

(15,16). Both of these factors favor unilamellarity, consistent with experimental observations reported here. On the other hand, the effect of salts may be difficult to predict because of their complicated (and in many cases, uncertain) influence on interbilayer forces and membrane mechanical properties. For example, the addition of monovalent salt has been shown to reduce attractive van der Waals forces in neutral bilayers (17,18) but also decrease interbilayer separation (and thereby increase adhesion) in charged bilayers through screening effects (the Debye length decreases by three orders of magnitude between pure water and physiological salt concentration). Moreover, NaCl has been shown to increase the bending rigidity of POPC multilayers (19) but decrease the bending rigidity of POPC giant unilamellar vesicles (16). Divalent cations are even more complicated because of their ability to tightly bind acidic headgroups (20). In short, the proposed mechanism should be used with appropriate caution; we recommend an approach of experimentally validating the effect of any sample additive using the methods described here.

The presence of multilamellar structures in extruded vesicles has been sporadically reported in the literature, often evidenced by their clear experimental signature in scattering studies (9,13,21). Some factors that can potentially influence multilamellarity are the number of freeze-thaw cycles (22), membrane lipid composition (9), and modification of lipid headgroups (for example, by PEG polymers) (13,22–24). This work expands on these observations in several important ways. First, we present a general scattering model that enables robust quantification of the accessible lipid fraction from SANS or SAXS data, and we validate the model-dependent analysis with direct cryoEM imaging, a real-space technique that provides a straightforward means to assess lamellarity. Notably, imaging revealed a nested vesicle structure difficult to detect with scattering that seems to be a preferred outcome for some samples; the mechanism responsible for creating this structure is not immediately obvious and warrants further investigation. Second, by examining nine different neutral lipids, we find that although residual MLVs are generally present after extrusion, their abundance differs in a manner that likely depends on membrane mechanical properties and possibly other factors. Finally, we identify three methods for increasing the fraction of unilamellar vesicles: 1) adding small amounts of charged lipid; 2) decreasing solution ionic strength; and 3) reducing extrusion pore size. Practically, these findings highlight a major potential artifact in very commonly used experimental preparations and provide a complementary set of strategies for mitigating the problem of MLV contamination in extruded samples. In addition, they point toward a mechanism by which extrusion strips MLVs of their layers (or in many cases, fails to do so) that can be further explored with theory, simulation, and experiment.

SUPPORTING MATERIAL

Supporting Material can be found online at https://doi.org/10.1016/j.bpj.2019.09.006.

AUTHOR CONTRIBUTIONS

F.A.H., I.L., E.G.K., and M.N.W. designed the research. H.L.S., A.S., E.G.K., M.N.W., and F.A.H. conducted experiments. H.L.S., A.S., E.G.K., M.N.W., I.L., and F.A.H. analyzed data. F.A.H. and I.L. wrote the article. H.L.S., A.S., E.G.K., M.N.W., I.L., and F.A.H. revised the manuscript.

ACKNOWLEDGMENTS

We thank Alex Sodt for helpful discussions. F.A.H. and H.L.S. were supported by National Science Foundation grant MCB-1817929. I.L. and A.S. were supported by the National Institutes of Health/National Institute of General Medical Sciences (GM114282, GM124072, GM120351), the Volkswagen Foundation (grant 93091), and the Human Frontiers Science Program (RGP0059/2019). M.N.W. was supported by an endowment from the William Wheless III Professorship and acknowledges National Institutes of Health Shared equipment grants for the Polara (S10 RR16714) and K2 Summit (S10 OD016279) with additional support provided through the Structural Biology Center at The University of Texas Medical School at Houston. Access to the NGB30 SANS Instrument was provided by the Center for High Resolution Neutron Scattering, a partnership between the National Institute of Standards and Technology and the National Science Foundation under agreement DMR-1508249. SAXS measurements were supported by Department of Energy scientific user facilities at Oak Ridge National Laboratory, and DLS measurements were supported by the Biophysical Characterization Suite of the Shull Wollan Center at Oak Ridge National Laboratory.

SUPPORTING CITATIONS

References (25–35) appear in the Supporting Material.

REFERENCES

1. Nagle, J. F., and S. Tristram-Nagle. 2000. Structure of lipid bilayers. *Biochim. Biophys. Acta.* 1469:159–195.
2. Heberle, F. A., J. Pan, …, J. Katsaras. 2012. Model-based approaches for the determination of lipid bilayer structure from small-angle neutron and X-ray scattering data. *Eur. Biophys. J.* 41:875–890.
3. McMahon, H. T., and E. Boucrot. 2015. Membrane curvature at a glance. *J. Cell Sci.* 128:1065–1070.
4. Rawicz, W., K. C. Olbrich, …, E. Evans. 2000. Effect of chain length and unsaturation on elasticity of lipid bilayers. *Biophys. J.* 79:328–339.
5. Feigenson, G. W. 2009. Phase diagrams and lipid domains in multicomponent lipid bilayer mixtures. *Biochim. Biophys. Acta.* 1788:47–52.
6. Marsh, D. 2009. Cholesterol-induced fluid membrane domains: a compendium of lipid-raft ternary phase diagrams. *Biochim. Biophys. Acta.* 1788:2114–2123.
7. Marsh, D. 2010. Liquid-ordered phases induced by cholesterol: a compendium of binary phase diagrams. *Biochim. Biophys. Acta.* 1798:688–699.
8. Andersen, O. S., and R. E. Koeppe, II. 2007. Bilayer thickness and membrane protein function: an energetic perspective. *Annu. Rev. Biophys. Biomol. Struct.* 36:107–130.
9. Kučerka, N., J. Pencer, …, J. Katsaras. 2007. Curvature effect on the structure of phospholipid bilayers. *Langmuir.* 23:1292–1299.

10. Heberle, F. A., D. Marquardt, …, G. Pabst. 2016. Subnanometer structure of an asymmetric model membrane: interleaflet coupling influences domain properties. *Langmuir.* 32:5195–5200.
11. Doktorova, M., D. Harries, and G. Khelashvili. 2017. Determination of bending rigidity and tilt modulus of lipid membranes from real-space fluctuation analysis of molecular dynamics simulations. *Phys. Chem. Chem. Phys.* 19:16806–16818.
12. Rand, R. P., and V. A. Parsegian. 1989. Hydration forces between phospholipid bilayers. *Biochim. Biophys. Acta.* 988:351–376.
13. Nele, V., M. N. Holme, …, M. M. Stevens. 2019. Effect of formulation method, lipid composition, and PEGylation on vesicle lamellarity: a small-angle neutron scattering study. *Langmuir.* 35:6064–6074.
14. Loosley-Millman, M. E., R. P. Rand, and V. A. Parsegian. 1982. Effects of monovalent ion binding and screening on measured electrostatic forces between charged phospholipid bilayers. *Biophys. J.* 40:221–232.
15. Mertins, O., and R. Dimova. 2013. Insights on the interactions of chitosan with phospholipid vesicles. Part II: membrane stiffening and pore formation. *Langmuir.* 29:14552–14559.
16. Faizi, H. A., S. L. Frey, …, P. M. Vlahovska. 2019. Bending rigidity of charged lipid bilayer membranes. *Soft Matter.* 15:6006–6013.
17. Marra, J. 1986. Direct measurements of attractive van der Waals and adhesion forces between uncharged lipid bilayers in aqueous solutions. *J. Colloid Interface Sci.* 109:11–20.
18. Petrache, H. I., T. Zemb, …, V. A. Parsegian. 2006. Salt screening and specific ion adsorption determine neutral-lipid membrane interactions. *Proc. Natl. Acad. Sci. USA.* 103:7982–7987.
19. Pabst, G., A. Hodzic, …, P. Laggner. 2007. Rigidification of neutral lipid bilayers in the presence of salts. *Biophys. J.* 93:2688–2696.
20. Rand, R. P., and V. A. Parsegian. 1984. Physical force considerations in model and biological membranes. *Can. J. Biochem. Cell Biol.* 62:752–759.
21. Pabst, G., R. Koschuch, …, P. Laggner. 2003. Structural analysis of weakly ordered membrane stacks. *J. Appl. Cryst.* 36:1378–1388.
22. Kaasgaard, T., O. G. Mouritsen, and K. Jørgensen. 2003. Freeze/thaw effects on lipid-bilayer vesicles investigated by differential scanning calorimetry. *Biochim. Biophys. Acta.* 1615:77–83.
23. Kenworthy, A. K., S. A. Simon, and T. J. McIntosh. 1995. Structure and phase behavior of lipid suspensions containing phospholipids with covalently attached poly(ethylene glycol). *Biophys. J.* 68:1903–1920.
24. Hristova, K., and D. Needham. 1995. Phase behavior of a lipid/polymer-lipid mixture in aqueous medium. *Macromolecules.* 28:99–1002.
25. Kline, S. R. 2006. Reduction and analysis of SANS and USANS data using IGOR Pro. *J. Appl. Cryst.* 39:895–900.
26. Doktorova, M., F. A. Heberle, …, O. S. Andersen. 2019. Gramicidin increases lipid flip-flop in symmetric and asymmetric lipid vesicles. *Biophys. J.* 116:860–873.
27. Pencer, J., S. Krueger, …, J. Katsaras. 2006. Method of separated form factors for polydisperse vesicles. *J. Appl. Cryst.* 39:293–303.
28. De Gennes, P. G., and J. Prost. 1993. The Physics of Liquid Crystals, Second Edition. Oxford University Press, Oxford, UK.
29. Pabst, G., M. Rappolt, …, P. Laggner. 2000. Structural information from multilamellar liposomes at full hydration: full q-range fitting with high quality x-ray data. *Phys. Rev. E Stat. Phys. Plasmas Fluids Relat. Interdiscip. Topics.* 62:4000–4009.
30. Mastronarde, D. N. 2005. Automated electron microscope tomography using robust prediction of specimen movements. *J. Struct. Biol.* 152:36–51.
31. Zheng, S. Q., E. Palovcak, …, D. A. Agard. 2017. MotionCor2: anisotropic correction of beam-induced motion for improved cryo-electron microscopy. *Nat. Methods.* 14:331–332.
32. Kučerka, N., M. P. Nieh, and J. Katsaras. 2011. Fluid phase lipid areas and bilayer thicknesses of commonly used phosphatidylcholines as a function of temperature. *Biochim. Biophys. Acta.* 1808:2761–2771.
33. Kučerka, N., J. Gallová, …, J. Katsaras. 2009. Areas of monounsaturated diacylphosphatidylcholines. *Biophys. J.* 97:1926–1932.
34. Pan, J., F. A. Heberle, …, N. Kučerka. 2012. Molecular structures of fluid phase phosphatidylglycerol bilayers as determined by small angle neutron and X-ray scattering. *Biochim. Biophys. Acta.* 1818:2135–2148.
35. Pan, J., X. Cheng, …, J. Katsaras. 2014. The molecular structure of a phosphatidylserine bilayer determined by scattering and molecular dynamics simulations. *Soft Matter.* 10:3716–3725.

Biophysical Journal, Volume *117*

Supplemental Information

On the Mechanism of Bilayer Separation by Extrusion, or Why Your LUVs Are Not Really Unilamellar

Haden L. Scott, Allison Skinkle, Elizabeth G. Kelley, M. Neal Waxham, Ilya Levental, and Frederick A. Heberle

The Supporting Material for

On the mechanism of bilayer separation by extrusion; or, why your large unilamellar vesicles are not really unilamellar

Haden L. Scott, Allison Skinkle, Elizabeth G. Kelley, M. Neal Waxham, Ilya Levental, Frederick A. Heberle

consists of Materials and Methods, 5 tables, and 7 figures.

S1. MATERIALS and METHODS

Materials. Phospholipids 1-palmitoyl-2-oleoyl-sn-glycero-3-phosphocholine (POPC), 1-palmitoyl-2-oleoyl-sn-glycero-3-phospho-(1'-rac-glycerol), sodium salt (POPG), 1-palmitoyl-2-oleoyl-sn-glycero-3-phospho-L-serine, sodium salt (POPS), 1-stearoyl-2-oleoyl-sn-glycero-3-phosphocholine (SOPC), 1,2-dioleoyl-sn-glycero-3-phosphocholine (DOPC), 1,2-dieicosenoyl-sn-glycero-3-phosphocholine (diC20:1-PC), 1,2-dierucoyl-sn-glycero-3-phosphocholine (diC22:1-PC), 1,2-dilauroyl-sn-glycero-3-phosphocholine (DLPC), 1,2-dimyristoyl-sn-glycero-3-phosphocholine (DMPC), 1,1-dimyristoyl-sn-glycero-3-phospho-(1'-rac-glycerol), sodium salt (DMPG), 1,2-dipalmitoyl-sn-glycero-3-phosphocholine (DPPC), and chicken egg sphingomyelin were purchased from Avanti Polar Lipids (Alabaster, AL) as dry powders and used as supplied. The phospholipids were dissolved in HPLC-grade chloroform and stored at −80 °C until use. PBS buffer tablets were from AMRESCO (Solon, OH). Ultrapure H_2O was obtained from a High-Q (Wilmette, IL) or Milli-Q Millipore purification system (Burlington, MA). D_2O (99.9%) was from Cambridge Isotope Laboratories (Tewksbury, MA).

Sample preparation. Aqueous lipid dispersions at 20 mg/mL were prepared by first mixing appropriate volumes of lipid stocks in organic solvent with a glass Hamilton syringe. The solvent was evaporated with an inert gas stream followed by high vacuum overnight. The dry lipid film was hydrated above the lipid's main transition temperature for at least 1 h with intermittent vortex mixing. The resulting multilamellar vesicle (MLV) suspension was subjected to at least 5 freeze/thaw cycles using a −80 °C freezer, then extruded through a polycarbonate filter using a handheld mini-extruder (Avanti Polar Lipids) by passing the suspension through the filter 31 times. Unsaturated lipids were extruded at room temperature, and saturated lipids and sphingomyelin were extruded at ~10 °C above their main transition temperature. Because different measurement techniques have different optimal concentration ranges, samples were diluted with water or buffer prior to measurement as described below. Samples were typically measured within a few days of preparation.

Dynamic Light Scattering (DLS). Samples were diluted with filtered water to ~ 0.1 mg/mL for DLS measurement in a Brookhaven BI-200SM system equipped with a HeNe laser (Brookhaven Instruments, Holtsville, NY). Typical instrument settings were: goniometer angle 90°; laser power 30 mW; aperture 200 μm; total measurement time 4 min. The vesicle size and polydispersity index reported in Table S2 were obtained from a cumulant analysis performed automatically by the instrument software.

Small-angle X-ray Scattering (SAXS). Vesicle samples for small-angle X-ray scattering (SAXS) measurements were prepared at 20 mg/mL as described above and measured using a Rigaku BioSAXS-2000 home source system (Rigaku Americas, The Woodlands, TX) equipped with a HF007 copper rotating anode, a Pilatus 100K 2D detector, and an automatic sample changer. SAXS data were collected at a fixed sample-to-detector distance (SDD) using a silver behenate calibration standard, with a typical data collection time of 30 min for MLVs and 3 h for LUVs. The one-dimensional scattering intensity $I(q)$ [$q = 4\pi \sin(\theta)/\lambda$, where λ is the X-ray wavelength and 2θ is the scattering angle relative to the incident beam] was obtained by radial averaging of the corrected 2D image data, an operation that was performed automatically using Rigaku SAXSLab software. Data were collected in 10-minute frames with each frame processed

separately to assess radiation damage; there were no significant changes in the scattering curves over time. Background scattering from water or buffer collected at the same temperature was subtracted from each frame, and the background-corrected $I(q)$ from the individual frames was then averaged, with the standard deviation taken to be the measurement uncertainty and used in weighted least-squares analyses described below.

Small-angle Neutron Scattering (SANS). SANS experiments were performed on the NG7 and NGB30 30m SANS instruments at the NIST Center for Neutron Research (NCNR). Data were collected using a neutron wavelength of 6 Å and wavelength spread ($\Delta\lambda/\lambda$) of 0.13. Measurements were made with sample-to-detector distances (SDD) of 1 m, 4 m, and 13 m. Additional low q data were collected with a lenses configuration that used a neutron wavelength of 8.09 Å and SDD of either 13 m or 15 m depending on the instrument. The configurations provided access to an approximate q-range of 0.001 $Å^{-1} < q < 0.4$ $Å^{-1}$, where q is as described above except λ refers to the neutron wavelength. Data were collected for 1-3 h depending on the vesicle concentration and were corrected for empty cell and instrument background using the IGOR Pro Macros provided by NIST (1).

Vesicles for SANS experiments were prepared at 10 mg/mL or 20 mg/mL as described above. Some samples were also diluted to 2 mg/mL for SANS measurements to minimize the structure factor from inter-vesicle interactions and better determine the vesicle radius and polydispersity at low q.

Scattering model. Scattering data were analyzed following (2,3) with modifications described here. The experimentally observed scattering intensity from a vesicle suspension can be expressed as the product of a single-bilayer vesicle form factor $P(q)$ and a structure factor $S(q)$ that accounts for density correlations between different bilayers (e.g., the stacked bilayers in a multilamellar vesicle):

$$I(q) = q^{-2}P(q)S(q)\,. \qquad Eq.S1$$

Pencer et al. (4) showed that, for a polydisperse vesicle suspension whose sizes follow a Schulz distribution, $P(q)$ is well-approximated by

$$P(q) \approx P_V(R_m, \sigma, q)|F_B(q)|^2\,, \qquad Eq.S2$$

where R_m is the average vesicle radius, σ is the relative size polydispersity, and

$$P_V(R_m, \sigma, q) = 8\pi^2 {R_m}^2 \sigma^4 (1+\sigma^{-2})(2+\sigma^{-2}) \times \left[1 - \frac{\left(1+4q^2{R_m}^2\sigma^4\right)^{-\frac{1}{2\sigma^2}} \cos\left((2+\sigma^{-2})\tan^{-1}(2qR_m\sigma^2)\right)}{1+4q^2{R_m}^2\sigma^4}\right]. \qquad Eq.S3$$

Equation S2 is valid provided the vesicle radius is much larger than the bilayer thickness. P_V was set to unity in SAXS analyses because vesicle size does not influence SAXS data within the experimental q range of this study.

The flat bilayer scattering amplitude $F_B(q)$ in Eq. S2 accounts for density correlations within a single bilayer, normal to the plane of the bilayer (i.e., the lipid bilayer structure). We model F_B using a symmetric six-slab volume probability distribution with separate components for the lipid headgroups, combined CH and CH_2 groups of the hydrocarbon chains, and terminal CH_3 groups at the bilayer midplane (2):

$$F_B(q) = \frac{2e^{-\frac{(q\sigma_S)^2}{2}}}{qD_H A_L V_T V_W (V_C - 2V_T)} \Big| V_T\{b_W(A_L D_H - V_H)(V_C - 2V_T) + V_W b_H (V_C - 2V_T) - V_W A_L D_H (b_C - 2b_T)\} \sin\left(\frac{qV_C}{A_L}\right) + V_T(V_C - 2V_T)(b_W V_H - b_H V_W) \sin\left(qD_H + \frac{qV_C}{A_L}\right) + V_W A_L D_H (b_C V_T - b_T V_C) \sin\left(\frac{2qV_T}{A_L}\right)\Big| . \qquad Eq.S4$$

In Eq. S4, V_C, V_H, V_T, and V_W are the molecular volumes of the lipid hydrocarbon chains, headgroup, terminal methyl, and water, respectively, with corresponding scattering factors b_C, b_H, b_T, and b_W (Table S1). To mimic the smoothing effects of thermal disorder, the step-like volume probability profile was convoluted with a Gaussian of width σ_S = 2.8 Å. Explicit bilayer structural parameters include the area per lipid A_L and the headgroup thickness D_H; additional structural parameters are derived from fitted model parameters, the most important of which are the total (Luzzati) bilayer thickness $D_B = 2(V_C + V_H)/A_L$ and the hydrocarbon thickness $2D_C = 2V_C/A_L$. Because of the large number of model parameters, we constrained V_T (53 $Å^3$) and the width of the headgroup region D_H (6 Å for X-ray data, 10 Å for neutron data unless otherwise stated) to improve the robustness of the fitting routine.

When two or more bilayers are stacked as in an MLV, correlations between the lamellae modulate the scattering according to Bragg's law. The resulting Bragg reflections appear in reciprocal space at multiples of the interlamellar repeat distance *d*, i.e. $q_m = m2\pi/d$ (*m* = 1, 2, 3…), and can be accounted for with a structure factor

$$S_N(q) = N + 2\sum_{k=1}^{N-1}(N-k)\cos(kqd)\, exp[-(dq/2\pi)^2\eta\{\gamma + \ln(\pi k)\}] , \qquad Eq.S5$$

where *N* is the number of bilayers in the stack, γ is Euler's constant, and $\eta = \pi k_B T/2d^2\sqrt{Bk_c}$ is the Caillé parameter, which is related to bilayer undulations and depends on the bulk modulus of compression *B* (5) the bilayer bending rigidity k_c, and the absolute temperature *T* (k_B is the Boltzmann constant). The width of the Bragg peaks is essentially controlled by η and is the result of several types of disorder and crystalline defects that have been thoroughly described elsewhere (3,6).

To account for heterogeneity in the number of stacked lamellae in a vesicle suspension (3), we use a modified exponential distribution in which the relative probability of finding a vesicle with *N* lamellae is given by

$$w_N(\lambda) = \begin{cases} w_1 , & N = 1 \\ e^{-\lambda N}, & N > 1 \end{cases} . \qquad Eq.S6$$

The distribution parameter λ is inversely related to the average number of lamellae, and the relative probability w_1 of a unilamellar vesicle (N = 1) is a separate parameter; this is a purely empirical modification of the exponential distribution to improve the fit quality. The ensemble-averaged structure factor that is inserted into Eq. S1 is given by

$$\langle S(q) \rangle = \sum_{N=1}^{N_{max}} S_N(q) w_N(\lambda) \; / \sum_{N=1}^{N_{max}} w_N(\lambda) \; , \qquad Eq.S7$$

where the (otherwise infinite) sum is truncated at a maximum number of layers governed by a cumulative probability cutoff *p,*

$$N_{max} = \lceil -\log(1-p)/\lambda \rceil . \qquad Eq.S8$$

We used a value of p = 0.999 for all analyses presented in this work. The ensemble-averaged number of lamellae $\langle N \rangle$ is obtained from the modified distribution as

$$\langle N \rangle = \sum_{N=1}^{N_{max}} N \, w_N(\lambda) \; / \sum_{N=1}^{N_{max}} w_N(\lambda) \; , \qquad Eq.S9$$

and the externally accessible lipid fraction is calculated as

$$f_{acc} = (2\langle N \rangle)^{-1} . \qquad Eq.S10$$

With this definition, a perfectly unilamellar sample has f_{acc} = 0.5. Finally, two useful metrics are the number fraction n_N and mass fraction (relative to the total lipid mass) m_N of vesicles with N lamellae:

$$n_N = w_N(\lambda) \; / \sum_{N=1}^{N_{max}} w_N(\lambda) , \qquad Eq.S11$$

$$m_N = N \, w_N(\lambda) \; / \sum_{N=1}^{N_{max}} N \, w_N(\lambda) . \qquad Eq.S12$$

Scattering analysis. Scattering data were fit using the model described in the previous section, implemented in a nonlinear least-squares routine using custom code written in Mathematica v11.3.0 (Wolfram Research, Champaign, IL). In most cases the adjustable parameters were A_L, V_C, η, d, λ, and w_1, in addition to a constant background and arbitrary scale factor. We found empirically that the most reliable results were obtained by varying the transformed parameter $\Lambda =$

λ^{-1} in a line search and refining the remaining adjustable parameters with a Levenberg-Marquardt algorithm included in Mathematica NonlinearModelFit function.

The robustness of the fitting routine was examined via Monte Carlo error estimation of parameter uncertainties. Briefly, experimental I(q) data were fitted with splines to produce a smooth curve, from which 500 synthetic I(q) datasets were generated by adding Gaussian noise with a standard deviation equal to the q-dependent measurement uncertainties determined during data reduction. The synthetic datasets were fit as described above to generate distributions of the best fit parameters, from which standard deviations were calculated. Table S4 shows the parameter mean values μ, standard deviations σ, and relative errors σ/μ for POPC vesicles hydrated in PBS buffer and extruded with a 100 nm pore size filter. The parameter uncertainty calculated from best fit values obtained from a set of sample replicates is in all cases larger than that calculated for each individual sample from a set of synthetic Monte Carlo replicates, demonstrating that the uncertainty arising from sample-to-sample variation overwhelms the uncertainty inherent to the model fitting.

Cryo-electron Microscopy (CryoEM). To cryopreserve vesicles, 4 μL of a 1 mg/mL sample were applied to a Quantifoil 2/2 carbon coated 200 mesh copper grid that was glow-discharged for 1 min at 15 mA in a Pelco Easi-Glow discharge device. After manual blotting, the grids were plunged into liquid ethane cooled with liquid N_2. Cryo-preserved grids were stored in liquid N_2 until use. Samples were coded prior to preservation and all sample preparation and image collection was accomplished by an investigator blind to the sample composition.

Image collection was accomplished at approximately 2 μm under focus on a FEI Polara G2 operated at 300 kV equipped with a Gatan K2 Summit direct electron detector operated in photon counting mode. Data collection was performed in a semi-automated fashion using Serial EM software operated in low-dose mode (7). Briefly, areas of interest were identified visually and 8x8 montages were collected at low magnification (2400x) at various positions across the grid and then individual areas were marked for automated data collection. Data was collected at 2.51 Å/pixel. Movies of 30 dose-fractionated frames were collected at each target site with the total electron dose being kept to < 20 $e^{-}/Å^2$. Dose-fractionated movies were drift-corrected with MotionCor2 (8).

Cryo-electron Microscopy data analysis. The extent of multillamellarity in LUV preparations was calculated from cryoEM images. For each sample, 120-190 vesicles from at least six images were measured and the number of lamellae manually counted. For preparations that resulted in formation of nested vesicles (i.e. smaller vesicles inside larger vesicles without characteristic interlamellar spacing), diameters of inner nested vesicles were recorded. f_{acc} was calculated in multilamellar vesicles with the assumption that each layer of the MLV had a diameter of 8 nm smaller than the preceding layer. The final calculations were almost insensitive to reasonable variations in this parameter.

SUPPORTING TABLES

Table S1 Volumes and scattering factors of lipids used in this study: V_H, headgroup volume; V_C, hydrocarbon volume; b_H^X, headgroup X-ray scattering factor; b_H^N, headgroup neutron scattering factor; b_C^X, hydrocarbon X-ray scattering factor; b_C^N, hydrocarbon neutron scattering factor. X-ray scattering factors are calculated as the total number of electrons of the constituent atoms (neglecting the q-dependence), and neutron scattering factors are calculated as the sum of atomic neutron scattering lengths of the constituent atoms.

Lipid	T [ºC]	V_H [Å^3]	b_H^X [e$^-$]	b_H^N [fm Å^{-3}]	V_C [Å^3]	b_C^X [e$^-$]	b_C^N [fm Å^{-3}]
DLPC[a]	25	331	164	60.072	656.5	178	-25.782
	30	331	164	60.072	659.8	178	-25.782
DMPC[a]	30	331	164	60.072	768.9	210	-29.11
	35	331	164	60.072	772.8	210	-29.11
DPPC[a]	50	331	164	60.072	897.5	242	-32.438
POPC[a]	25	331	164	60.072	920.5	256	-26.624
	35	331	164	60.072	929.8	256	-26.624
SOPC[a]	25	331	164	60.072	973.5	272	-28.288
DOPC[b]	30	331	164	60.072	972.3	270	-20.81
Di20:1PC[b]	30	331	164	60.072	1079.7	302	-24.138
Di22:1PC[b]	30	331	164	60.072	1189.9	334	-27.466
DMPG/D_2O[c]	35	291	166	95.91	766.5	210	-29.11
POPG/H_2O[c]	25	291	166	75.09	914.9	256	-26.624
POPS/H_2O[d]	25	278	172	88.189	920.5	256	-26.624
Egg-SM/H_2O[e]	50	274	150	47.441	883.7	240	-24.96

[a]ref. 9; [b]ref. 10; [c]ref. 11; [d]ref. 12; [e]Norbert Kučerka, personal communication.

Table S2 Vesicle size and polydispersity index (PDI) obtained from DLS, and bilayer structural parameters obtained from SAXS analysis (parameters are defined in Section S1). Values in italics were constrained.

Composition	Solvent	T [°C]	Extrusion pore size [nm]	*DLS parameters* diam. [nm]	PDI	*SAXS parameters* $\langle N \rangle$	f_{acc}	n_1	m_1	d [Å]	η	V_L [Å^3][a]	A_L [Å^2]
POPC	H_2O	25	unextruded	7600	0.13	3.42	0.15	0.29	0.09	62.6	0.09	1257	*65*
			1000	272	0.27	1.63	0.31	0.69	0.42	63.0	0.08	1257	64.7
			400	295	0.30	1.62	0.31	0.68	0.42	63.0	0.08	1257	64.6
			200	182	0.16	1.35	0.37	0.77	0.57	63.0	0.09	1256	64.4
			100	143	0.10	1.21	0.41	0.83	0.68	63.2	0.10	1255	64.3
				126	0.17	1.18	0.42	0.85	0.72	63.8	0.08	1253	63.3
			50	108	0.09	1.09	0.46	0.92	0.85	63.4	0.11	1255	64.2
			30			1.03	0.48	0.97	0.94	64.5	0.07	1255	63.8
	PBS	25	unextruded			6.74	0.07	0.15	0.02	63.9	0.07	1264	*65*
						17.8	0.03	0.05	0.00	62.6	0.07	1252	*65*
						7.81	0.06	0.13	0.02	63.8	0.08	1265	*65*
			100	134	0.25	1.51	0.33	0.70	0.47	62.0	0.09	1262	64.8
				138	0.12	1.40	0.36	0.75	0.54	62.4	0.08	1263	64.6
				136	0.15	1.34	0.37	0.77	0.57	62.2	0.08	1262	64.3
				115	0.12	1.41	0.35	0.75	0.53	62.3	0.08	1262	64.4
	D_2O	35	100	116	0.03	1.11	0.45	0.90	0.82	63.7	0.11	1261	65.3
POPC/POPG 95/5	H_2O	25	unextruded	495	0.29	1.18	0.42	0.87	0.73	71.5	0.44	1257	65.0
			1000	353	0.20	1.16	0.43	0.88	0.75	73.6	0.44	1256	64.7
			400	261	0.15	1.16	0.43	0.88	0.76	74.4	0.53	1255	64.4
			200	172	0.10	1.07	0.47	0.93	0.87	75.3	0.52	1253	63.9
			100	135	0.10	1.03	0.48	0.97	0.93	*75*	*0.52*	1253	63.8
			50	103	0.09	1.02	0.49	0.99	0.97	*75*	*0.52*	1252	63.7
			30	72	0.08	1.01	0.49	0.99	0.98	*75*	*0.52*	1253	63.8
POPC/POPG 98/2	D_2O	35	100	130	0.04	1.03	0.49	0.97	0.95	71.6	*0.40*	1262	65.5
POPC/POPG 96/4				125	0.11	1.02	0.49	0.98	0.96	76.8	*0.50*	1262	65.5
POPC/POPG 94/6				120	0.10	1.02	0.49	0.98	0.95	*75*	*0.50*	1261	65.4
POPC/POPG 92/8				130	0.09	1.03	0.48	0.98	0.95	*75*	*0.50*	1261	65.3
POPC/POPG 90/10				117	0.12	1.03	0.49	0.97	0.95	*75*	*0.50*	1261	65.4
POPC/POPG 98/2	PBS	25	100	127	0.21	1.36	0.37	0.76	0.56	63.3	0.11	1264	64.7
POPC/POPG 96/4				113	0.21	1.18	0.42	0.85	0.72	66.6	0.17	1262	64.5
POPC/POPG 94/6				118	0.24	1.14	0.44	0.88	0.77	70.7	0.25	1262	64.5
POPC/POPG 92/8				94	0.27	1.11	0.45	0.91	0.82	71.8	0.25	1262	64.4
POPC/POPG 90/10				100	0.28	1.10	0.46	0.91	0.83	*75*	0.38	1261	64.5
POPC/POPS 98/2	H_2O	25	100	115	0.24	1.01	0.50	0.85	0.98	*63*	*0.2*	1253	63.3
POPC/POPS 96/4				108	0.21	1.00	0.50	0.99	1.0	*63*	*0.2*	1252	63.1
POPC/POPS 94/6				115	0.14	1.00	0.50	1.0	1.0	*63*	*0.2*	1252	63.0
POPC/POPS 92/8				108	0.31	1.00	0.50	1.0	1.0	*63*	*0.2*	1250	62.9
POPC/POPS 90/10				118	0.24	1.00	0.50	1.0	1.0	*63*	*0.2*	1249	62.7
DLPC	H_2O	30	unextruded	1600	0.15	12.7	0.04	0.08	0.01	57.7	0.10	990	*62.1*
			100	113	0.08	1.14	0.44	0.88	0.77	58.6	0.13	994	62.1
DMPC		30	unextruded	1800	0.23	10.2	0.05	0.10	0.01	62.4	0.09	1100	*58*
			100	102	0.06	1.10	0.45	0.91	0.82	63.7	0.15	1099	58.0
DPPC		50	unextruded	2300	0.005	5.9	0.08	0.16	0.03	65.3	0.10	1237	*62.4*
			100	172	0.18	1.09	0.46	0.92	0.84	67.8	0.16	1227	62.4
Egg-SM		50	unextruded	522	0.36	1.18	0.42	0.98	0.84	62.5	0.05	1178	61.0
			100	114	0.04	1.02	0.49	0.99	0.97	66.1	0.02	1177	60.6
SOPC		25	unextruded			7.5	0.07	0.13	0.02	65.2	0.05	1302	61.8
			100	127	0.03	1.20	0.42	0.84	0.70	65.8	0.08	1308	63.1
				128	0.19	1.27	0.39	0.80	0.62	65.6	0.08	1309	63.3
DOPC		30	unextruded	1500	0.005	9.4	0.05	0.10	0.01	62.4	0.07	1294	*68.9*
			100	130	0.12	1.16	0.43	0.86	0.74	63.4	0.10	1302	68.9
Di20:1-PC		30	unextruded	2620	0.17	5.2	0.10	0.19	0.04	65.4	0.06	1412	*67.1*
			100	120	0.05	1.08	0.46	0.93	0.86	67.2	0.06	1412	67.1
Di22:1-PC		30	unextruded	2000	0.005	9.2	0.05	0.11	0.01	69.3	0.03	1515	*64.8*
			100	140	0.02	1.21	0.41	0.83	0.68	70.3	0.04	1520	64.8

[a]The lipid hydrocarbon volume V_C was allowed to vary from the initial input values given in Table S1; we report the best-fit total lipid volume $V_L = V_C + V_H$ here.

Table S3 Vesicle size distribution and bilayer structural parameters obtained from SANS analysis (parameters are defined in Section S1). Values in italics were constrained.

Composition	Solv.	T [°C]	Extrusion pore size [nm]	Conc. [mg/mL]	*SANS parameters*								
					diam. [nm]	σ	$\langle N \rangle$	f_{acc}	n_1	m_1	d [Å]	η	A_L [Å^2]
DLPC	D_2O	25	400	20	342	0.13	2.45	0.20	0.54	0.22	58.1	0.18	*61*
				2	614	0.17	3.00	0.17	0.44	0.15	57.5	0.22	*61*
			200	20	205	0.26	1.44	0.35	0.77	0.54	59.1	0.19	*61*
				2	131	0.30	1.64	0.30	0.67	0.41	57.0	0.28	*61*
			100	20	71	0.42	1.20	0.42	0.85	0.71	58.0	0.40	61.0
				2	87	0.26	1.25	0.40	0.83	0.67	57.8	0.33	59.9
			50	20	51	0.31	1.03	0.48	0.97	0.94	63.4	0.82	62.8
				2	53	0.26	1.06	0.47	0.95	0.89	*62*	*0.8*	60.5
			30	20	49	0.33	1.05	0.48	0.96	0.91	63.0	0.64	61.3
				2	53	0.28	1.09	0.46	0.94	0.86	61.0	0.62	*61*
DMPC	D_2O	35	400	20	711	0.16	2.35	0.21	0.60	0.26	61.8	0.24	59.7
			200		131	0.35	1.47	0.34	0.78	0.53	62.5	0.23	59.5
			100		96	0.32	1.20	0.42	0.91	0.76	62.1	0.11	*59*
			50		59	0.33	1.09	0.46	0.96	0.88	67.1	0.56	*59*
			30		52	0.33	1.08	0.46	0.96	0.89	*63*	0.52	*59*
DMPC	D_2O/ 100 mM NaCl	35	100	10	92	0.30	1.19	0.42	0.84	0.71	62.4	0.45	59.1
DMPC/DMPG 98/2					92	0.33	1.40	0.36	0.80	0.57	68.1	0.57	59.3
DMPC/DMPG 95/5					91	0.30	1.14	0.44	0.90	0.79	98.5	1.17	58.7
DMPC/DMPC 90/10					86	0.29	1.16	0.43	0.87	0.76	113.9	0.75	58.3
DMPC/DMPG 80/20					81	0.33	1.13	0.44	0.89	0.79	126.8	0.72	58.7
DMPC/DMPG 50/50					108	0.32	1.13	0.44	0.89	0.80	138.3	0.71	59.8
DMPG					87	0.34	1.06	0.47	0.94	0.89	156.3	0.43	62.6

Table S4 Uncertainty in fitted model parameters for SAXS data from POPC hydrated in PBS buffer and extruded with a 100 nm pore size filter (parameters are defined in Section S1). Columns 2-4 correspond to the average μ, standard deviation σ, and percent error (defined here as $100\,\sigma/\mu$) from four replicate samples. The remaining columns show the same information calculated for each of the individual samples using Monte Carlo error estimation as described in the Materials and Methods.

	Sample replicates (N = 4)			Sample 1 MC replicates (N = 500)			Sample 2 MC replicates (N = 500)			Sample 3 MC replicates (N = 500)			Sample 4 MC replicates (N = 500)		
Param	μ	σ	% err	μ	σ	% err	μ	σ	% err	μ	σ	% err	μ	σ	% err
A_L	64.5	0.2	**0.3**	64.8	0.10	**0.15**	64.6	0.05	**0.08**	64.4	0.05	**0.08**	64.5	0.05	**0.08**
V_C	931.2	0.5	**0.05**	930.7	0.3	**0.03**	931.8	0.15	**0.02**	931.1	0.13	**0.01**	931.7	0.14	**0.02**
η	0.082	0.008	**9.5**	0.093	0.003	**2.8**	0.082	0.002	**2.0**	0.077	0.002	**2.2**	0.079	0.002	**2.1**
d	62.2	0.2	**0.3**	61.98	0.015	**0.02**	62.40	0.01	**0.02**	62.20	0.01	**0.02**	62.27	0.01	**0.02**
$\langle N \rangle$	1.42	0.07	**4.9**	1.51	0.006	**0.4**	1.40	0.003	**0.2**	1.34	0.002	**0.2**	1.41	0.003	**0.2**
f_{acc}	0.35	0.02	**4.8**	0.33	0.001	**0.4**	0.36	0.001	**0.2**	0.37	0.001	**0.2**	0.35	0.001	**0.2**
n_1	0.74	0.03	**3.7**	0.70	0.004	**0.5**	0.74	0.002	**0.5**	0.77	0.002	**0.2**	0.74	0.002	**0.3**
m_1	0.53	0.04	**8.4**	0.46	0.004	**0.9**	0.53	0.002	**0.5**	0.57	0.002	**0.4**	0.53	0.002	**0.5**

Table S5 Lipid and membrane physical properties and correlation coefficients with the externally accessible lipid fraction f_{acc} for extruded 100 nm vesicles in pure water.

Lipid	f_{acc}	Number of carbons per chain	Number of double bonds	Area per lipid [Å^2]	Hydrocarbon thickness [Å]	Melting temp. [°C]	Bending modulus [k_BT][c]
DLPC	0.44	12	0	62.1	21.3	7.0	25.8
DMPC	0.45	14	0	58.0	26.5	23.9	34.7
DPPC	0.46	16	0	62.4	28.7	41.4	34.1
ESM	0.49	17	1	60.6	29.8	39.0	41.8
POPC	0.42	17	1	63.3	29.1	–2.0	24.3
SOPC	0.40	18	1	63.3	30.9	6.0	26.4
r[a]		**–0.13**	**–0.18**	**–0.56**	**–0.03**	**0.84**	**0.91**
DOPC	0.43	18	2	68.9	28.2	–17.3	18.3
di20:1-PC	0.46	20	2	67.1	32.2	–4.3	21.1
di22:1-PC	0.41	22	2	64.8	36.7	13.2	26.9
r[b]		**–0.24**	**–0.22**	**–0.31**	**–0.20**	**0.55**	**0.61**

[a]correlation coefficient considering only mixed-chain and fully saturated lipids; [b]correlation coefficient considering all lipids; [c]obtained from atomistic simulations in (13) except for diC20:1-PC and diC22:1-PC, which were from a personal communication (M. Doktorova).

SUPPORTING FIGURES

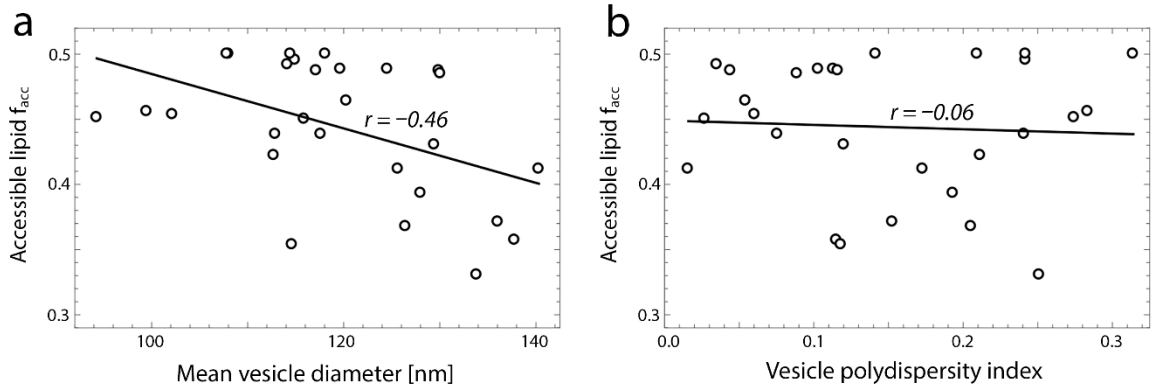

Figure S1 DLS is insensitive to multilamellar vesicles in extruded samples. For vesicles extruded with a 100 nm pore size filter (Table S2), the fraction of externally accessible lipid f_{acc} determined from SAXS is weakly correlated with the mean vesicle diameter (Pearson correlation coefficient r = –0.46) and is uncorrelated with the vesicle polydispersity index (r = –0.06) measured with dynamic light scattering, as shown in panels *a* and *b*, respectively.

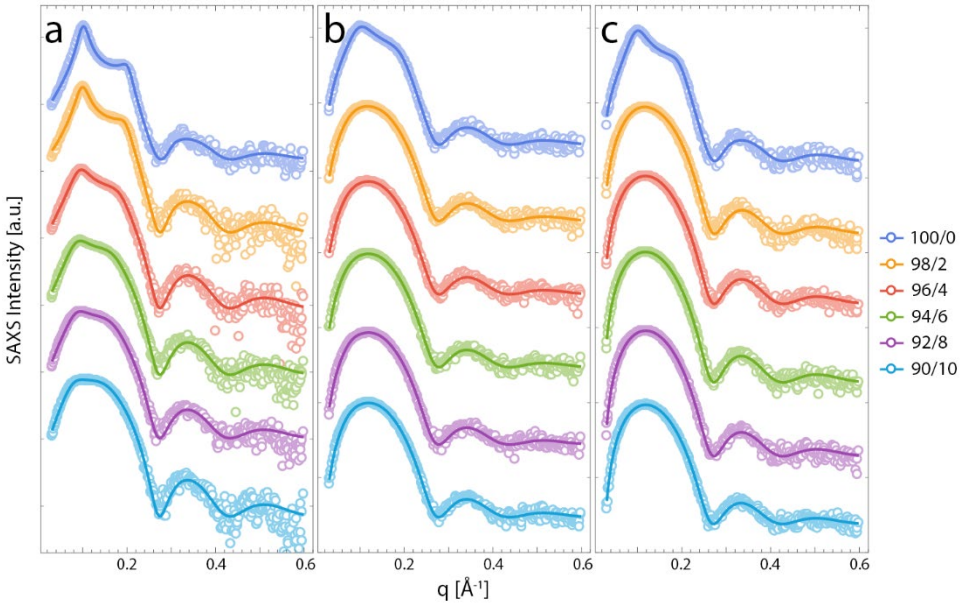

Figure S2 SAXS data from extruded POPC vesicles with increasing amounts of charged lipid. (a), POPC/POPG mixtures (molar ratios indicated in the legend) dispersed in PBS buffer at 20 mg/mL and measured at 25°C. (b), POPC/POPG mixtures (molar ratios indicated in the legend) dispersed in D_2O at 20 mg/mL and measured at 35°C. (c), POPC/POPS mixtures (molar ratios indicated in the legend) dispersed in H_2O at 20 mg/mL and measured at 25°C. All vesicles were extruded with a 100 nm pore size filter. Experimental data are shown as open circles and the fitted model is shown as a solid line. Values for fitted parameters are given in Table S2.

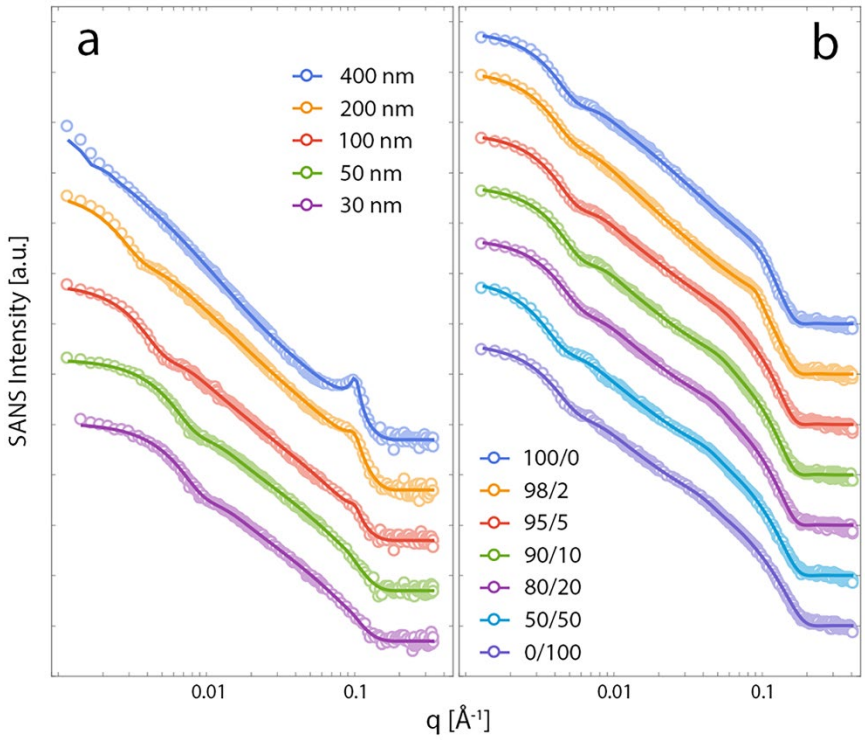

Figure S3 SANS data from DMPC vesicles. (a), DMPC dispersed in D_2O at 20 mg/mL, extruded with pore size indicated in legend, and measured at 35°C (b), DMPC/DMPG mixtures (molar ratios indicated in the legend) dispersed in D_2O/100 mM NaCl at 10 mg/mL, extruded with a 100 nm pore size filter, and measured at 35°C. Experimental data are shown as open circles and the fitted model is shown as a solid line. Values for fitted parameters are given in Table S3.

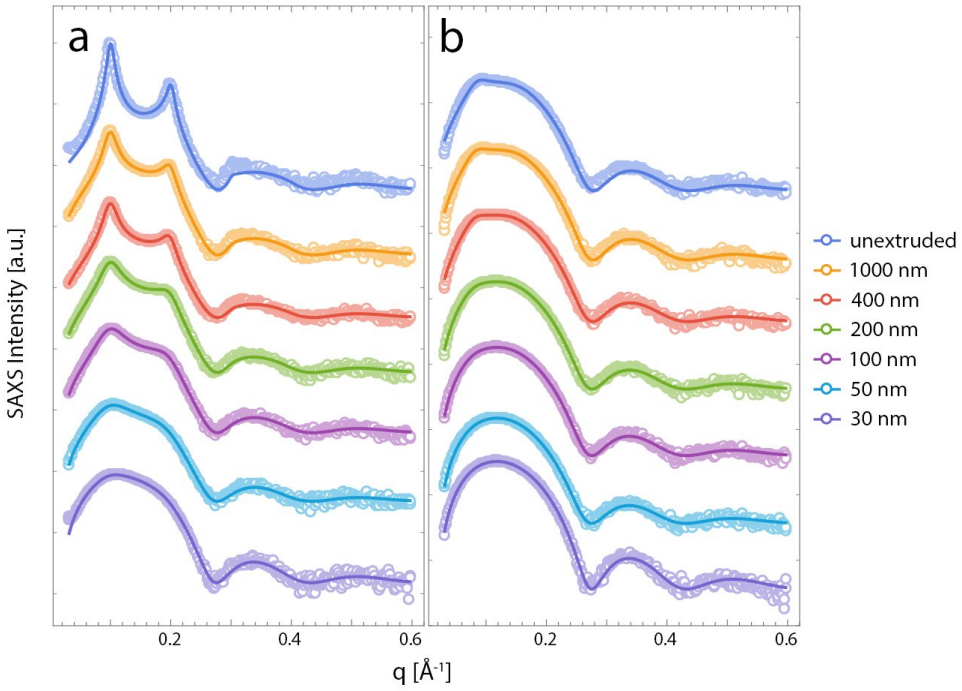

Figure S4 SAXS data from POPC vesicles extruded through different pore sizes. POPC (panel *a*) or POPC/POPG 95/5 molar mixture (panel *b*) dispersed in H_2O at 20 mg/mL, extruded with pore size indicated in legend, and measured at 25°C. Experimental data are shown as open circles and the fitted model is shown as a solid line. Values for fitted parameters are given in Table S2.

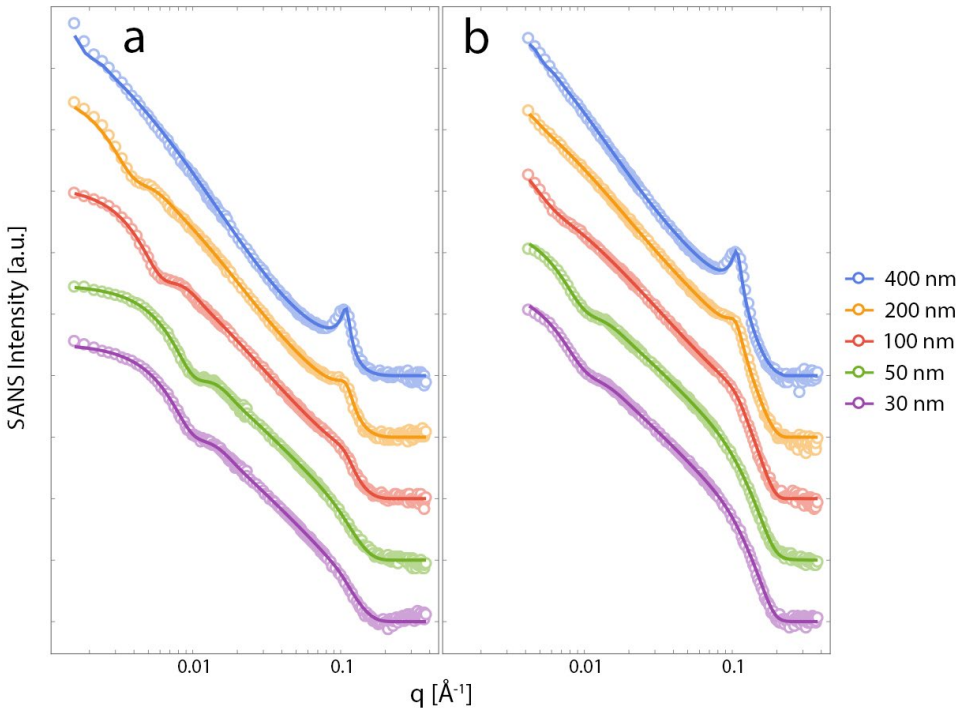

Figure S5 SANS data from DLPC vesicles extruded through different pore sizes. DLPC at 2 mg/mL (panel *a*) or 20 mg/mL (panel *b*) dispersed in D_2O, extruded with pore size indicated in legend, and measured at 25°C. Experimental data are shown as open circles and the fitted model is shown as a solid line. Values for fitted parameters are given in Table S3.

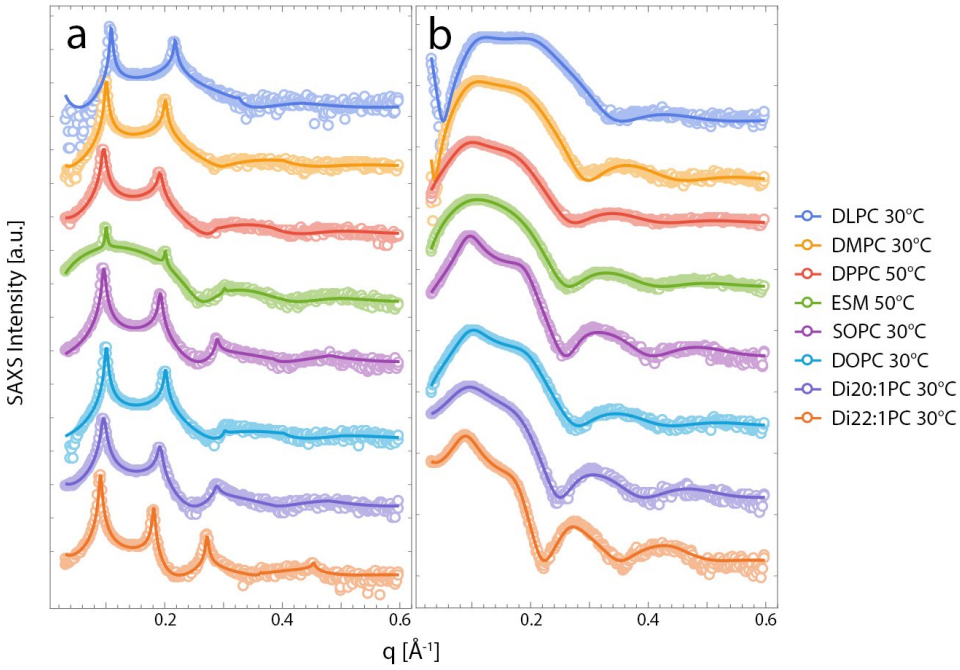

Figure S6 SAXS data from extruded vesicles composed of neutral lipids in the fluid phase. Lipid dispersed in H_2O at 20 mg/mL and measured at the temperature indicated in the legend either prior to extrusion (panel *a*) or after extrusion with a 100 nm pore size filter (panel *b*). Experimental data are shown as open circles and the fitted model is shown as a solid line. Values for fitted parameters are given in Table S2.

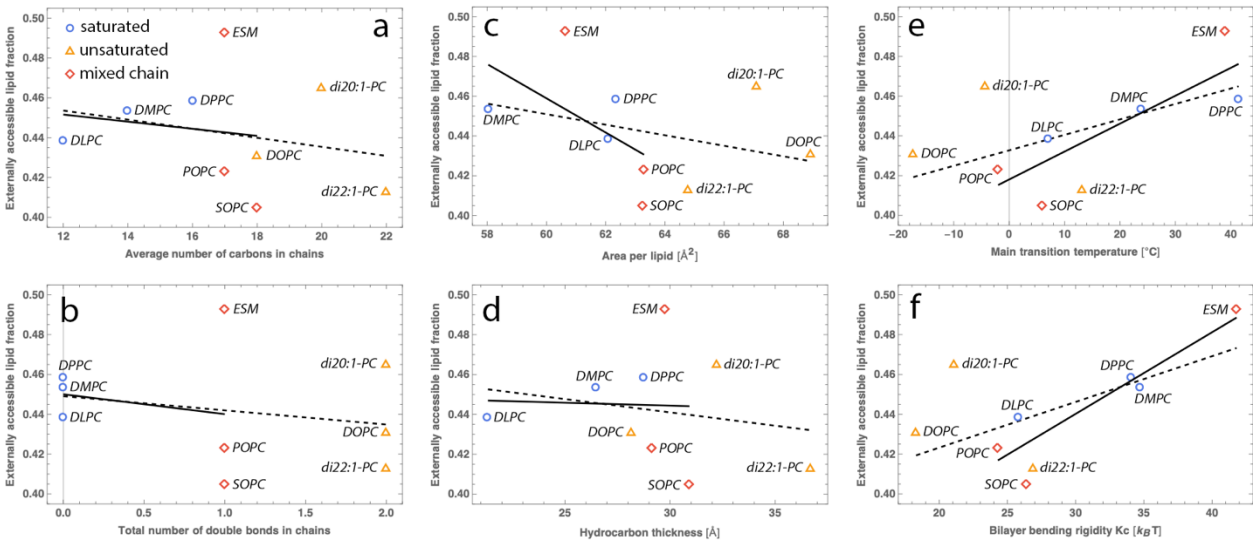

Figure S7 Average vesicle lamellarity is correlated with membrane bending rigidity. Shown for various neutral lipids hydrated in water and extruded through 100 nm pores (as indicated in the plots) is the trend between f_{acc} and different membrane physical parameters: (a) the average number of carbons in the chains; (b) the total number of double bonds in the chains; (c) the area per lipid (Table S2); (d) the bilayer's hydrocarbon thickness ($2D_C = 2V_C/A_L$, Table S2); (e) the main transition temperature; and (f) the membrane bending rigidity determined from atomistic molecular simulations. The dashed and solid lines are linear trendlines with and without the di-monounsaturated lipids (i.e., DOPC, di20:1-PC, and di22:1-PC), respectively; in both cases, the strongest correlation is with the bending rigidity. Parameter values and correlation coefficients are given in Table S5.

REFERENCES

1. S. R. Kline. 2006. Reduction and analysis of SANS and USANS data using IGOR Pro. J. Appl. Crystallogr. 39:895-900.
2. Doktorova, M., Heberle, F. A., Marquardt, D., Rusinova, R., Sanford, R. L., Peyear, T. A., Katsaras, J., Feigenson, G. W., Weinstein, H., and O. S. Andersen. 2019. Gramicidin Increases Lipid Flip-Flop in Symmetric and Asymmetric Lipid Vesicles. Biophys. J. 116:860-873.
3. Pabst, G., Koschuch, R., Pozo-Navas, B., Rappolt, M., Lohner, K., and P. Laggner. 2003. Structural analysis of weakly ordered membrane stacks. J. Appl. Crystallogr. 36:1378-1388.
4. Pencer, J., Krueger, S., Adams, C. P., and J. Katsaras. 2006. Method of separated form factors for polydisperse vesicles. J. Appl. Crystallogr. 39:293-303.
5. De Gennes, P. G., and J. Prost. 1993. The Physics of Liquid Crystals. 2nd ed. Oxford University Press, Oxford, UK.
6. Pabst, G., Rappolt, M., Amenitsch, H., and P. Laggner. 2000. Structural information from multilamellar liposomes at full hydration: full q-range fitting with high quality x-ray data. Phys. Rev. E 62:4000-4009.
7. D. N. Mastronarde. 2005. Automated electron microscope tomography using robust prediction of specimen movements. J. Struct. Biol. 152:36-51.

8. Zheng, S. Q., Palovcak, E., Armache, J. P., Verba, K. A., Cheng, Y., and D. A. Agard. 2017. MotionCor2: anisotropic correction of beam-induced motion for improved cryo-electron microscopy. Nat. Methods 14:331-332.
9. Kučerka, N., Nieh, M. P., and J. Katsaras. 2011. Fluid phase lipid areas and bilayer thicknesses of commonly used phosphatidylcholines as a function of temperature. Biochim. Biophys. Acta 1808:2761-2771.
10. Kučerka, N., Gallova, J., Uhrikova, D., Balgavy, P., Bulacu, M., Marrink, S. J., and J. Katsaras. 2009. Areas of monounsaturated diacylphosphatidylcholines. Biophys. J. 97:1926-1932.
11. Pan, J., Heberle, F. A., Tristram-Nagle, S., Szymanski, M., Koepfinger, M., Katsaras, J., and N. Kučerka. 2012. Molecular structures of fluid phase phosphatidylglycerol bilayers as determined by small angle neutron and X-ray scattering. Biochim. Biophys. Acta 1818:2135-48.
12. Pan, J., Cheng, X., Monticelli, L., Heberle, F. A., Kučerka, N., Tieleman, D. P., and J. Katsaras. 2014. The molecular structure of a phosphatidylserine bilayer determined by scattering and molecular dynamics simulations. Soft Matter 10:3716-3725.
13. Doktorova, M., Harries, D., and G. Khelashvili. 2017. Determination of bending rigidity and tilt modulus of lipid membranes from real-space fluctuation analysis of molecular dynamics simulations. Phys. Chem. Chem. Phys. 19:16806-16818.